



Halloysite reinforced 3D-printable geopolymers

Ranjbar, Navid; Kuenzel, Carsten; Gundlach, Carsten; Kempen, Paul; Mehrali, Mehdi

Published in:
Cement and Concrete Composites

Link to article, DOI:
[10.1016/j.cemconcomp.2022.104894](https://doi.org/10.1016/j.cemconcomp.2022.104894)

Publication date:
2023

Document Version
Publisher's PDF, also known as Version of record

[Link back to DTU Orbit](#)

Citation (APA):
Ranjbar, N., Kuenzel, C., Gundlach, C., Kempen, P., & Mehrali, M. (2023). Halloysite reinforced 3D-printable geopolymers. *Cement and Concrete Composites*, 136, Article 104894.
<https://doi.org/10.1016/j.cemconcomp.2022.104894>

General rights

Copyright and moral rights for the publications made accessible in the public portal are retained by the authors and/or other copyright owners and it is a condition of accessing publications that users recognise and abide by the legal requirements associated with these rights.

- Users may download and print one copy of any publication from the public portal for the purpose of private study or research.
- You may not further distribute the material or use it for any profit-making activity or commercial gain
- You may freely distribute the URL identifying the publication in the public portal

If you believe that this document breaches copyright please contact us providing details, and we will remove access to the work immediately and investigate your claim.



Halloysite reinforced 3D-printable geopolymers

Navid Ranjbar^{a,*}, Carsten Kuenzel^b, Carsten Gundlach^c, Paul Kempen^{d,e}, Mehdi Mehrali^{a,**}

^a Department of Civil and Mechanical Engineering, Technical University of Denmark, 2800, Kgs Lyngby, Denmark

^b Department of Civil and Environmental Engineering, Imperial College London, London, UK

^c Department of Physics, Technical University of Denmark, 2800, Kgs Lyngby, Denmark

^d DTU Nanolab, National Center for Nano Fabrication and Characterization, Technical University of Denmark, 2800, Kgs Lyngby, Denmark

^e Department of Health Technology, Technical University of Denmark, 2800, Kgs Lyngby, Denmark

ARTICLE INFO

Keywords:

3D printing
Geopolymer
Halloysite
Rheology
Mechanical properties

ABSTRACT

This study investigates the role of halloysite nanotube as a mineral-based thixotropic admixture to 3D printable geopolymer mortar. The first part of this paper focuses on the fundamental characterization of the thermal evolution of halloysite at 30–1000 °C. In the second part, we show how the calcination and concentration of halloysite influence the fresh and hardened properties of 3D-printable geopolymer mortar. It was found that regardless of thermal treatment, using only 1–2 wt% halloysite can significantly increase the rheological properties and buildability of the mortars without compromising their mechanical strength. However, the setting time of geopolymer only accelerated when highly reactive dehydroxylated halloysite was used. Compared with mold-cast specimens, the mechanical properties of 3D-printed specimens were lower at early ages due to their higher surface dehydration; however, the gap became closer over time.

1. Introduction

Concrete 3D-printing is an emerging technology that potentially overturns traditional construction by increasing geometrical freedom and saving industry on time, labor costs, formwork, and safety [1,2]. Large-scale 3D printing with concrete has been increasingly under development over the last decade [3]. Despite its great potential, printing using conventional concretes poses several new challenges. From a rheological point of view, compared with mold-casting practices, extra flowability is needed to meet the requirement of the pumping process and the material deposition without plugging the nozzle. However, as the formwork's lateral confinement must be tolerated directly by the printable concrete itself, the materials need a fast structural build-up to remain in place after the deposition [4]. While high-resolution printing limits the maximum aggregate size, resulting in high proportions of binder and reduced aggregate packing [4–6]. Besides, the increased surface area exposed to desiccation in the absence of formwork imposes higher thermal cracks than the conventional practice [7]. As a result, different admixtures have been used to modify the rheological properties of concrete to successfully execute pumping and deposition while achieving desirable hardened properties [8–10]. The

studies not only focus on Portland cement-based composites but also on other cementitious materials, such as geopolymer, that can integrate additional functionality into building elements and thus offset additional technology costs.

Geopolymers are ceramic-like inorganic polymers consisting of chains of mineral molecules linked with covalent bonds, produced from a wide range of natural and waste resources of aluminosilicates mixed with an alkaline activator [11]. Their unique properties include the potential for quick setting while attaining high early and final mechanical strength [12], and superior chemical and thermal resistance [13], making them a low-CO₂ alternative to Portland cement for various applications. Geopolymerization can be described by two semi-simultaneous steps, I) dissolution and II) gelation/polycondensation. First, the activation solution with high OH⁻ concentration breaks the covalent bonds of the amorphous phases of aluminosilicate particles, releasing Si and Al ions into the solution. These ions form reactive precursors with many Si–OH and Al–OH groups that further condense to form Si–O–Al and Si–O–Si bonds, resulting in 3D aluminosilicate gel. While, the negative charge of aluminate anions is balanced by counter ions available in the activation solution [14]. At a micro level, the reaction speed is dissimilar for different precursors, and

* Corresponding author.

** Corresponding author.

E-mail addresses: naran@dtu.dk (N. Ranjbar), meme@dtu.dk (M. Mehrali).

<https://doi.org/10.1016/j.cemconcomp.2022.104894>

Received 26 September 2022; Received in revised form 2 November 2022; Accepted 10 December 2022

Available online 17 December 2022

0958-9465/© 2022 The Authors. Published by Elsevier Ltd. This is an open access article under the CC BY license (<http://creativecommons.org/licenses/by/4.0/>).

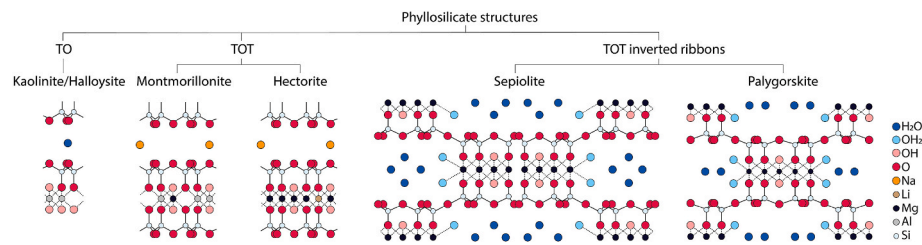


Fig. 1. Classification of crystal structures of clay minerals and ball and stick model structures of some common clays.

Table 1

Oxide composition and LOI of FA and HA.

	SiO ₂	Al ₂ O ₃	Fe ₂ O ₃	CaO	TiO ₂	K ₂ O	SO ₃	P ₂ O ₅	LOI [%]
FA	53,1	20,5	11,4	6,3	1,7	2,6	1,4	1,9	0,5
HA	54,1	44,4	0,8	0,1	0,1	0,4	–	–	14,9

Al–O bonds are easier to break and have a faster initial dissolution rate than those of Si–O bonds [12,15,16]. This causes massive precipitation of a rich Al metastable gel, “Gel 1”, at the beginning of the gelation to produce a microstructural framework and coats unreacted/partially-reacted grain boundaries [17–19]. Acting as a coat, the formation of *Gel 1* limits the unreacted particles’ access to the alkaline medium, thus slowing down the reaction rate [12,17]. However, due to diffusion, Si from aluminosilicates becomes available gradually and densifies *Gel 1* into a more stable Si-rich gel, called “Gel 2” [17,18,20]. This dense gel consists of high Si connectivity incorporated with tetrahedral aluminum linked with compensating cations and raises a multiplication percolation path in the structural framework [20,21].

Mechanically, the formation of *Gel 1* contributes to a fast (but weak) evolution of the elastic modulus, and *Gel 2* causes a significant increase in mechanical strength [20]. However, at the early stages of the reaction, the temporal evolution of mechanical strength is not only a function of chemical bonds but also the colloidal inter-particle interactions. This evolution is partially/fully reversible when it is subjected to shearing. As a result, geopolymers can sustain certain stress levels without flowing while behaving as a liquid-like material when subjected to applied stress more than the strength of the particles’ network interaction [22]. This initial internal strength is often insufficient to avoid material deformation under the applied forces, e.g., its own weight and nozzle pressure. Thus, reactive and unreactive additives have been used in the basic formulation to intensify the rheological properties. The increase in internal strength can be on a chemical or physical basis. The hardening rate can be retarded or accelerated by altering the content of reactive precursors (e.g., replacing fly ash (FA) with slag or dehydroxylated clay) or by adding chemical admixtures (e.g., sucrose as a retarder [23]). On the other side, unreactive fillers such as attapulgite clay [24] and polymeric fibers [25] are used as thickener agents with less influence on the reaction. The efficiency of unreactive fillers is a function of their specific surface area, surface charge, and surface functional groups.

Nanoclays are known as environmentally friendly rheology modifiers to cementitious material due to their water absorption properties and the flocculated structure they may adopt. Roughly, 30 various types of nanoclays exist in terms of their mineralogical and chemical composition. They are composed of one or two-dimensionally extended layers of octahedral (Al³⁺, Fe²⁺, Fe³⁺, or Mg²⁺) and tetrahedral (Si⁴⁺) sheets that are stacked over each other, and the interlayer may contain water molecules [26]. According to the specific arrangement of their tetrahedral (T) and octahedral (O), nanoclays can be categorized into two major types: i) tetrahedral–octahedral (TO), ii) tetrahedral–octahedral–tetrahedral (TOT) fully stacked or TOT partially stacked structure, see Fig. 1 [27]. The most popular examples of TO sheet arrangement group of nanoclays can refer to kaolinite, halloysite,

and serpentine. For the second category (TOT), we can refer to montmorillonite, hectorite, and synthetic laponite nanoclays for TOT fully stacked, and sepiolite and palygorskite for TOT partially stacked structures which have fibrous or needle-like structures with channels [27, 28]. Of all, halloysite nanotube (HA), is of more interest as a rheology modifier agent due to its unique morphology, high surface reactivity, and hydrophilic nature that makes it well dispersed in aqueous solution [29,30]. HA (Al₂Si₂O₅(OH)₄·nH₂O) is naturally made of kaolin clay mineral sheets rolled several times with a thickness of about 18–22 nm and length of 0.5–10 μm [31,32]. Besides, HA is generally less reactive to both alkaline and acidic environment but is rendered much more reactive by thermal treatment. To this end, HA can be used as a reactive or unreactive filler.

We have recently shown a detailed rheological characterization of 3D printable fly ash-based geopolymer mortars focusing on early-stage structuration [22]. The current study aims to investigate the attribution of HA (and calcined HA) in two key factors of printability (printing window and buildability) and its long-term contribution to mechanical strength. To this end, the first part of this paper explores the effects of calcination on HA physicochemical properties. In the second part, less and highly reactive HAs were used as additives to 3D-printable FA-based geopolymer, and their contribution to early and hardened properties is discussed. The microstructure and mechanical properties of the 3D-printed specimens are compared with their mold-cast counterparts.

2. Materials and method

2.1. Raw materials

The aluminosilicate source to make geopolymer was class F FA obtained from HOFOR Amagerværket, a thermal power plant in Copenhagen, Denmark. The FA had a particle size of d₁₀ = 2 μm, d₅₀ = 12 μm and d₉₀ = 35 μm. The HA, commercially known as ULTRA HalloPure, was provided by I-Minerals, Inc., based in Vancouver, Canada, with a mining site in north-central Idaho, USA. ULTRA HalloPure from I-Minerals was chosen for this research because of the high degree of purity (+90% halloysite <10% kaolinite). To increase reactivity, a muffle furnace was used for the calcination of the HA. The temperature was increased from 25 °C to 800 °C with a heating rate of 5 °C/min⁻¹ and then kept for 2 h; afterwards, the powder was left in the furnace to cool down. The product was labeled as meta-halloysite (MHA). The oxide composition of the FA was measured using an S8 Tiger 3 KW X-RAY Fluorescence analysis instrument, and the manufacturer provided the result for HA, see Table 1.

Dust-free silica sand with a high quartz content (obtained by Dansk, Denmark) was used as filler. The particle size distribution of the used sand was in the range of 90–250 μm.

The alkali activator used in this study was a mixture of sodium silicate (7.8–8.2 wt% SiO₂, and 26.6–27.0 wt% Na₂O; supplied by S. Sørensen- Thisted) and 8 M sodium hydroxide solutions with the mass ratio of 15:2. Sodium hydroxide was provided in pellet form by INOVYN. This mass ratio was used based on our previous study [22].

2.2. Geopolymer mortar preparation

Dry sand and FA were initially mixed with a constant mass ratio of sand:FA = 1.5 for 0.5 min. HA/MHA, in the range of 0–15 wt% of the FA, was gradually added to the dry mixture using a snap ball tea strainer. The activation solution with a constant mass ratio of activator:FA = 0.66 was mixed with an electric mixer for 5 min to obtain fresh geopolymer mortar. In this study, the only varying parameter was the content of HA/MHA.

2.3. Characterizations

2.3.1. X-ray diffraction analysis (XRD)

The amorphous and crystalline phases of the as-received and calcined HAs were characterized with a HUBER G670 X-ray powder diffractometer (Germany) in the 2 θ range 3–100° in steps of 0.005° using CuK α 1 radiation ($\lambda = 1.54056 \text{ \AA}$) for 10 min, 40 kV, and 40 mA. All measurements were carried out at room temperature. Data were collected in transmission mode from a rotating flat plate sample inclined 45° relative to the primary beam. For quantification, HA powders were blended with 15 wt% anatase (Titanium(IV)) oxide powder, 99.8% trace metals basis- Sigma-Aldrich) as standard internal following the previous study [22]. A total of 1 g powder sample was mixed with 2 mL of 2propanol and homogenized by vibration mill-Retsch MM400 for 10 min. The amorphous phases were quantified using Rietveld quantitative analysis at X'Pert Highscore Plus software by adjusting the scale factors, background, zero shift, lattice cell, and peak shape parameters of W, V, and U for the pattern fitting.

TG analysis was carried out using TGA Q500 (TA instrument, USA) in the range of 30 °C–1000 °C with a heating rate of 10 °C.min⁻¹ under a constant airflow of 60 mL min⁻¹.

2.3.2. Fourier transform infrared (FTIR) spectroscopy

FTIR spectroscopy was performed with a PerkinElmer Spectrum 100 (USA) equipped with an attenuated total reflectance (ATR). Data were collected from 4000 to 400 cm⁻¹ for 16 scans at a resolution of 4 cm⁻¹.

2.3.3. Particles size and Brunauer–Emmett–Teller (BET) surface area analysis

Particle size distribution of powders was measured using Malvern 3000 laser diffraction particle size analyzer (Malvern Instruments Ltd., UK). Here the particle was first dispersed in Na-polyphosphate and then sonicated for 40 s before the measurements. Particle sizes were measured by comparing the light scattering profiles with Mie theory, using refractive index = 1,4 and absorption index = 0,01. Notably, this measurement technique is more applicable for particles with low aspect ratios.

The BET-specific surface area was analyzed using the Autosorb-iQ analyzer (Quantachrome Instruments USA). Before the measurements, samples were degassed at 70 °C for 15 h. 7 points method was used to analyze the data.

2.3.4. Dissolution reactivity

Dissolution reactivity of HA was measured by mixing 1 g of the powder with 100 ml 8 M sodium hydroxide solution and stirring for 24 h at 60 °C [33,34]. After the dissolution, solid residue was separated from the liquid by centrifuging the suspension at 6000 rpm for 3 min using Thermo Scientific Sorvall RC 6 Plus centrifuge. Then the solid residue was mixed with ~200 mL of deionized water, shaken manually for 1 min, and centrifuged as mentioned above. This process was repeated

three times. Finally, the residue was dried at 250 °C and weighted. However, initial measurements showed that HA formed a complex colloidal suspension during washing, and a large number of the particles were unwantedly removed. This caused an overestimation of HA's reactivity. Thus, a similar experiment was performed while stirring time was limited to 30 s. It was assumed that the weight loss of the second experiment was only due to the colloidal effect, not the dissolution.

2.3.5. Microscopy

Transmission electron microscopy (TEM) was performed using FEI Tecnai T12 Biotwin (Thermo Fisher Scientific, Waltham, MA, USA) operating at 120 kV. Images were taken using an Orius CCD camera equipped with Digital Micrograph (Gatan, Pleasanton, USA). To prepare the TEM samples, halloysite nanotubes were first ultrasonically dispersed in MilliQ water for 15 min. Then, 5 μ l of the suspension was deposited onto freshly glow discharged 200 mesh formvar coated nickel TEM grids and left for 5 min for some solid particles to settle, and the rest of the suspension was removed.

Scanning electron microscopy (SEM) in backscattered mode was performed on fractured surfaces of geopolymer mortars using a Phenom ProX scanning electron microscope (Phenom-World Inc., Netherlands).

2.3.6. Rheological characterization

Rheological characterization of geopolymer mortars was performed on an Anton Paar Physica MCR 502 rheometer using a stainless steel parallel plate system with a 25 mm diameter (PP25) and a gap of 2 mm. The environmental temperature was adjusted at 25 °C using P-PTD200 and H-PTD200 temperature control systems. The data were recorded with the software Rheoplus/32, version 1.23.403 (Anton Paar GmbH).

2.3.7. Setting time

Using a manual Vicat needle setup, the setting time was measured according to ASTM-C191-19. In preliminary experiments, it was observed that the top layer of geopolymer hardened faster due to the evaporation of surface water, thus, causing heterogeneity in measurement. To reduce this effect, the surface of the samples was covered with a thin oil layer [33,34]. Three different samples were measured for each composition.

2.3.8. Printing procedure

Printability of the fresh geopolymer mortars was measured using an Engine S.R., HYREL 3D printer equipped with a piston-driven cartridge holding up to 60 mL and a nozzle with a rectangular orifice of 20 \times 3.6 mm. The device was controlled using Repetrel software.

For printing, fresh geopolymer mortar was poured into the cartridge and extruded 5 min after the first contact between FA and the activation solution. Two sets of samples were prepared using the printer. To assess the printing window and to prepare the samples for mechanical testing, the length and height of each printed layer were programmed to be 90 mm and 3.5 mm, respectively, and a total of six layers were printed continuously with a constant travel speed of 300 mm/min to form each specimen. To assess the buildability, layers of geopolymers with the length and height of 30 mm and 3.5 mm, respectively, were printed continuously on top of each other with a constant travel speed of 300 mm/min. The structure's maximum height before the collapse was considered the composition's buildability. The collapse was referred to when the bottom layers failed to sustain accumulative stress from the successive layers on top. At least three samples were prepared for each test.

2.3.9. X-ray micro-computed tomography (X-ray μ -CT)

Nikon XT H 225 ST (Nikon Metrology Inc, Brighton, MI, USA) X-ray μ -CT instrument was used to characterize the internal structures of mold-cast and 3D-printed specimens. The used parameters to set up the system can be summarized as 85 kV high voltage and a power of 25 W for the X-ray tube. The specimen was rotated 360° continuously while

acquiring 1571 images at different rotation angles in the instrument, and X-ray images were acquired with 0.5 s exposure on each projection. Samples were scanned twice to get different magnifications and fields of view. As a result, for determined positions of the X-ray sources, specimen, and detector, efficient pixel sizes of 38.6 μm and 89.7 μm were obtained. 3D volumes were then reconstructed using the systems reconstruction software based on an FDK implementation of a filtered back-projection algorithm resulting in a voxelated 3D volume where the length of each side of a voxel was equal to the efficient pixel size of 38.6 μm . Avizo was used for the post-processing of the reconstructed data.

2.3.10. Mechanical characterization

An Instron 5967 universal test machine with a maximum load capacity of 30 kN was used to measure the evolution of mechanical properties of the geopolymer mortars. The prismatic 3D printed specimens, as explained in subsection 2.3.8, were first used to measure the flexural strength, and later, the halved samples were used for compressive strength measurement. In addition to 3D-printed samples, conventional mold-cast specimens with dimensions of 150 \times 25 \times 25 mm and 25 \times 25 \times 25 were prepared for flexural and compressive testing, respectively. The early-age (3rd and 7th days) and long-term (28th day) compressive strengths were assessed with 10 kN and 30 kN load cells, respectively, at a pacing rate of 0.5 mm min⁻¹. Flexural strengths were measured on prismatic samples through three-point bending tests using a 10 kN load cell with a rate of 0.1 mm min⁻¹. Specimen's edges were slightly chamfered using sandpaper to avoid a pseudo fluctuation at the early steps of the measurement.

3. Results and discussion

3.1. Effects of thermal treatment on halloysite's structural and morphological properties

3.1.1. Structural changes

The structure and composition of clay minerals are changed by heat treatment. However, the actual temperature at which the changes occur varies greatly from one clay mineral group to another, depending on their structure, particle size, and heating regime. Based on the weight and structural changes of the HA upon thermal treatment, the activation process was divided into five main steps, see Fig. 2. In step I (~30–~120 °C), the halloysite underwent a mass loss associated with the evaporation of the major part of adsorbed or interlayer water, see Fig. 2b. Removing this water physically affects the interlayer spacing between alumina and silica layers, which shrinks from ~10 Å in hydrated halloysite to ~7 Å after complete dehydration [31,32]. In this study, the loss at step I was insignificant. This suggested that the used halloysite was initially almost dehydrated. In step II (~120–~350 °C), the mass was relatively stable, and the little loss was associated with removing the remaining interlayer water molecules. A similar structural arrangement was observed in XRD patterns of halloysite in stages I and II showing a 7 Å-type halloysite structure (JCPDS No. 29-1487, Al₂Si₂O₅(OH)₄) with a trace of kaolinite (JCPDS No. 29-1488, Al₂(Si₂O₅)(OH)₄), see Fig. 2c. At stage III, the halloysite was dehydroxylated, i.e., it lost its structural water, OH radicals in the structure reacted together to form water. The loss of these water molecules formed vacant lattice sites and eventuated a disordered halloysite phase. This process left a significant mass loss within the temperature range of

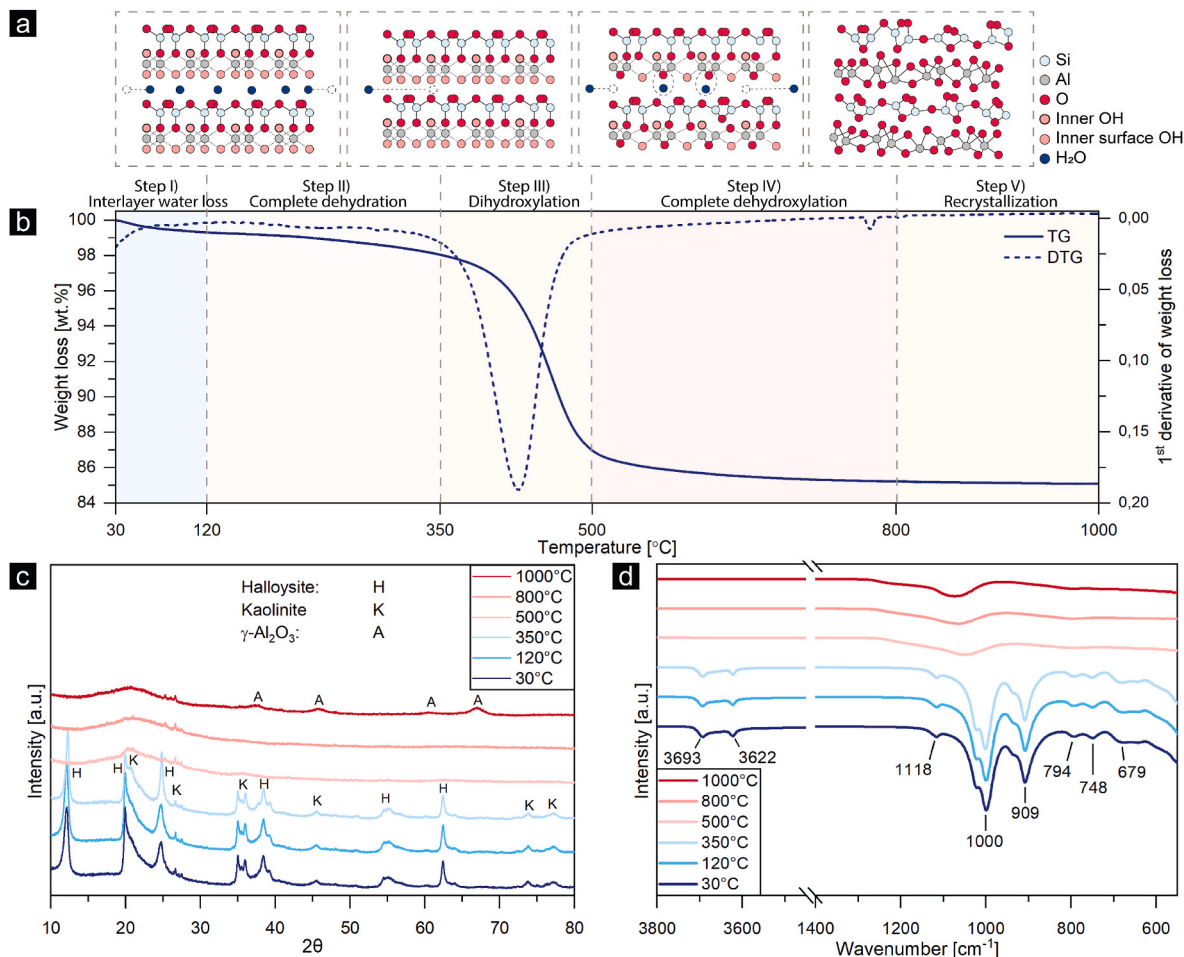


Fig. 2. a) Schematic model of halloysite dehydroxylation steps; b) TGA and DTG curves; c) XRD patterns; d) FTIR spectra.

Table 2
Particle size and dissolution reactivity of HA, MHA, FA, and sand.

	Particle size [μm]			BET [$\text{m}^2\cdot\text{g}^{-1}$]	Dissolution reactivity [%]	X-ray amorphous phases [%]
	d_{10}	d_{50}	d_{90}			
HA	0,2	0,4	2,4	32,4	48,6	32,8
MHA	1,8	12,0	45,6	30,2	79,2	92,1
Sand	27,3	45,9	72,2	2,0	1,9	
FA	2,2	11,9	36,4	4,0	40,0	

~350–~500 °C (fell off in the first derivative curve at ~430 °C) [31,32, 35]. The infrared spectra in Fig. 2d indicate disappearing bands attributed to O–H vibration of inner-surface hydroxyl groups at 3622 and 3693 cm^{-1} and the Al–O–H bending at 908 cm^{-1} linked with inner hydroxyl groups [32,36]. Furthermore, the broadened highest absorption in the IR spectrum of halloysite that linked to stretching vibration of Si–O–Si and reflected an increased structural disordering at this step [32,36]. This major structural change was also observed in XRD patterns by forming X-ray amorphous products, MHA, see Fig. 2c and Table 2. No significant mass loss of the halloysite was measured by increasing the temperature in the range of 500–800 °C, and the amorphous structure was almost retained, Step IV. However, this step is regarded as the complete dehydroxylation of the halloysite and the persistence of MHA. A further increase to 1000 °C, Step V, resulted in phase segregation in halloysite and crystallization of new phases, mainly low order (or nanocrystalline) $\gamma\text{-Al}_2\text{O}_3$ (JCPDS No. 001-077-0396, Al_2O_3), see Fig. 2b

[37].

3.1.2. Morphological variations

TEM images of unheated halloysite in Fig. 3a and b shows that the particles were typically cylindrical and contained hollow and open-ended core. After calcination, despite the particles undergoing a thermal decomposition at ~500 °C, they preserved their tubular geometry and structural integrity up to ~800 °C, see Fig. 3c and d. This observation is in agreement with previous studies [32,35]. However, as shown in Fig. 3d, the halloysite nanotubes were frequently sintered and aggregated at 800 °C (Note, the aggregation was not simply destroyed by the ultrasonic dispersion used for the TEM sample preparation described earlier). The growth in particle size of heat-treated halloysite confirmed this aggregation, see Fig. 3f. This aggregation also caused new levels of porosities, i.e., macro- and mesopores, from particle-to-particle interactions. A further increase to 1000 °C caused a

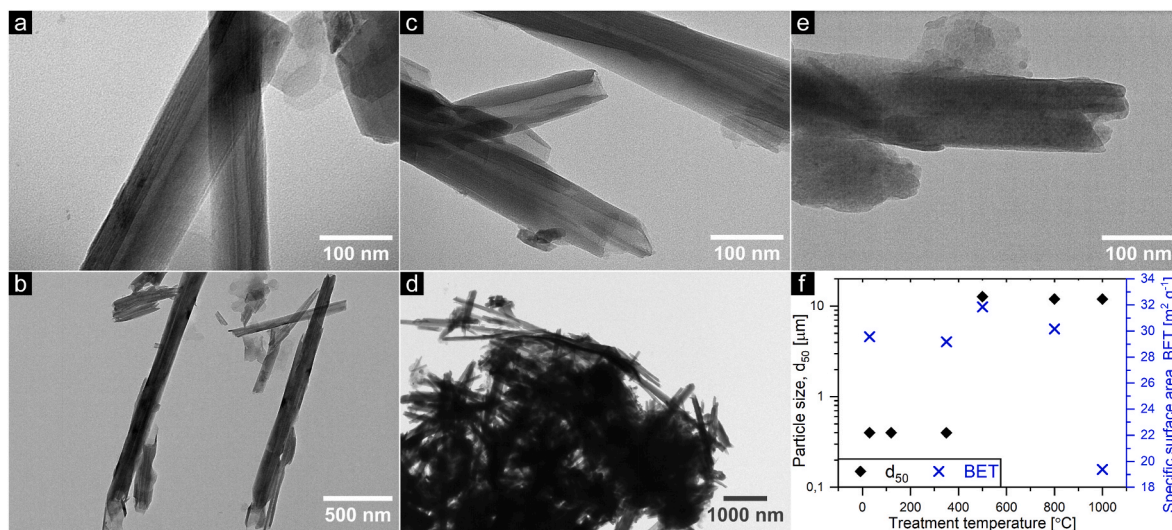


Fig. 3. TEM images of HA morphological changes upon heat treatment at a) 30 °C, b) 800 °C, and c) 1000 °C; aggregation status of HA nanotubes at d) 30 °C and e) 800 °C; f) changes in d_{50} and BET of HA particle at different pre-treatment temperatures.

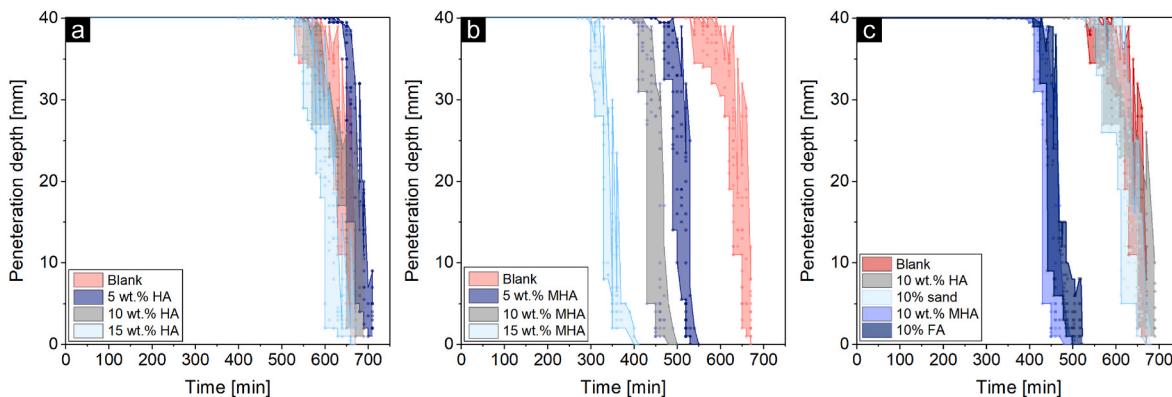


Fig. 4. Vicat setting time of geopolymer mortars containing different masses of a) HA, and b) MHA; c) comparing the setting time of the geopolymer mortars included 10 wt% HA/MHA with the reference compositions containing a similar mass of FA and sand.

substantial surface mottling and change in morphology of the calcined halloysite, see Fig. 3e. In addition, the BET was considerably decreased. This can be attributed to either sintering or formation of more stable phases with less surface area, or a combination of them.

In the following, as-received HA and completely dehydroxylated HA at 800 °C, MHA, were used as additives in fly ash-based geopolymer.

3.2. Setting time

Fig. 4a and b shows Vicat needle penetration test results for geopolymer mortars with different amounts of HA/MHA. Besides, the result for two reference geopolymer compositions substituting a similar mass of HA/MHA with sand (as an inert material) and FA (as a reactive material) is shown in Fig. 4c. The variation in setting time was almost negligible when different HA concentrations were added to the geopolymer mortar, see Fig. 4a. This behavior was comparable to that of the matrix containing only sand. This was initially unexpected because it was assumed that increasing the solid ratio by adding inert materials, thus providing more surface for precipitation of reaction product, should reduce the setting of the geopolymer matrices [12,38,39]. Interestingly, the variation of the specific surface area of the inert precursors was of almost no influence ($HA = 32,37 \text{ m}^2 \text{ g}^{-1}$ and $sand = 0,58 \text{ m}^2 \text{ g}^{-1}$). On the other side, increasing the MHA reduced the setting time of the geopolymer mortars, similar to the reference geopolymer that FA substituted HA, see Fig. 4b and c [30]. The increased reactivity of dehydroxylated HA explains this accelerated setting for geopolymerization, see Table 2, which can partially be due to the transformation of aluminium coordinate number from 6 to a combination of 4, 5, and 6, as well as the availability of more amorphous phases [12, 40–42]. A similar dissolution reactivity of HA and FA, and their different

behaviors for setting times was unexpected. As explained in Section 2.3.5, the experimental conditions were controlled to consider the unintentional removal of solid particles, despite the measurement could still be affected. It is also important to consider that the dissolution test was performed at 60 °C, which can increase the HAs reaction rate [33]. The latter is more likely to be the reason for the different behaviors of HA in the two experiments.

3.3. Experimental and numerical evaluation of the printability of geopolymer mortars

Fig. 5a shows the printing window of the geopolymer mortars with a resolution of 15 min as a function of HA/MHA content and time. The printing window of the unreinforced geopolymer mortar was 60 min after the mixing, and it was reduced significantly by adding HA and MHA. However, a minimum printing window of 30 min was secured for all the mixing compositions. Comparing Vicat setting times and printing windows show their large time gaps. This result is in agreement with the previous measurements [22,43]; however, this study shows that compositions with different setting times may have a similar printing window due to dissimilar kinetics of reactions and temporal inter-particle interactions.

The experimental setup used to measure the maximum height that mortars can carry before the collapse is shown in Fig. 5b. The data for different geopolymer mortars are presented in Fig. 5c. As observed, similar to other types of nano-clays, adding a small amount of HA substantially increased the geopolymers matrix's buildability [10,44,45]. This was because the water that normally lubricates particles and facilitates their rolling over each other under an applied force was absorbed partially by HA particles. Thus, inter-particle frictional forces

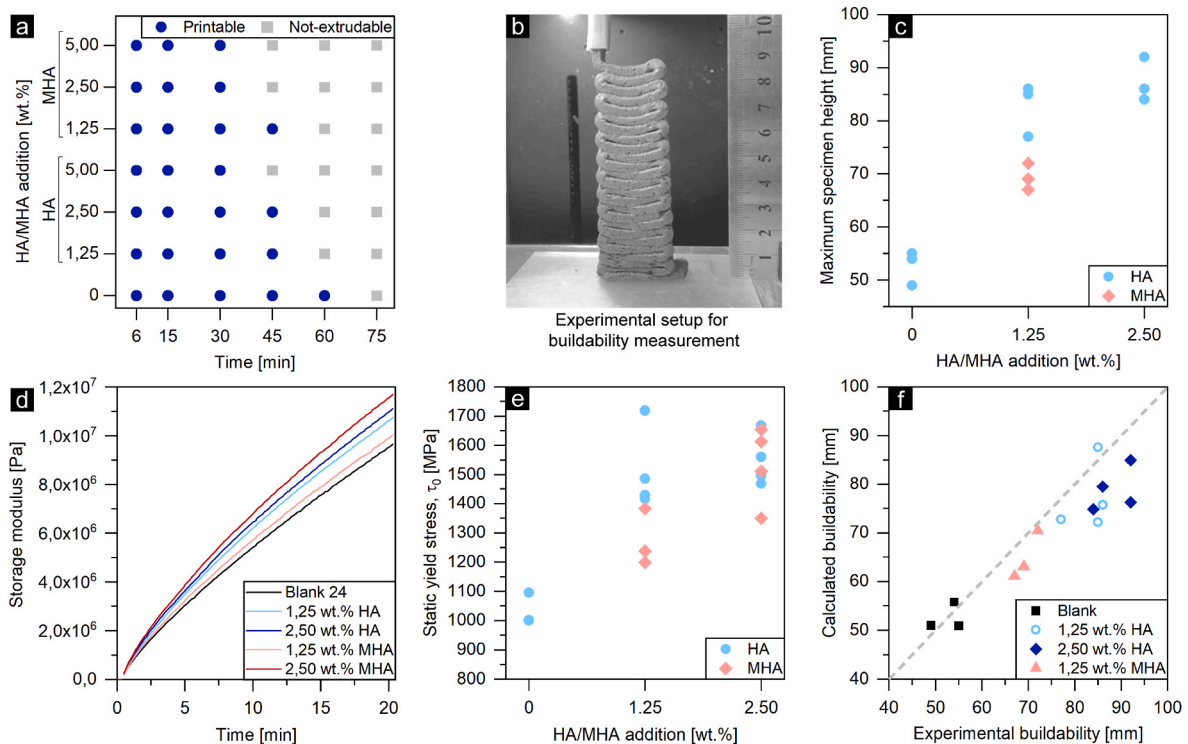


Fig. 5. a) printing window; b) experimental setup for measuring buildability; c) maximum printing height before the collapse; d) storage modulus as a function of time; e) static yield stress of the mortars; f) comparing buildability measured through experiment and theoretical approach proposed by Ref. [22].

were increased in the absence of water, and the matrix’s rheological properties were changed. The buildability of MHA matrices was lower than their corresponding HA mixes. This was an artifact, and caused by the gradual phase separation of MHA matrices during extrusion using the printer of this study. It can be explained that the reactive MHA particles acted as seeds for further nucleation [46], limiting the movement of solid particles. The aggregated MHA also intensified this effect. As a result, the matrix was not extruded uniformly, and the liquid:solid ratio was higher at the early layers. Thus they failed to sustain the gravitational forces from the top layers, and the buildability was reduced. This condition was exacerbated at compositions with higher MHA content (e.g., 2.5 wt%), and a large volume of the mortar remained not-extrudable inside the printer container. Fig. 5e shows the temporal evolution of storage modulus that used to estimate the static yield stress and buildability of the compositions after extrusion according to the procedure proposed in Ref. [22]; see the result in Fig. 5e and ef. As observed, there is a high agreement between the calculated buildability and the experimentally measured values. The estimation is slightly reduced at compositions containing a higher amount of HA, which is attributed to the formation of manufacturing-induced porosity during 3D printing of those compositions that correspondingly reduced their bulk density.

3.4. Physicomechanical characterization of hardened mortars

Fig. 6a shows that there is an optimum at ~2.5 wt% HA addition which the compressive strength of mold-cast geopolymers is at the maximum while further additions reverse the effect. Since HA is less reactive [37,47], the variation in compressive strengths for different concentrations of HA can be explained by the changes in the pore structure of the mortars. The HA particles act dominantly as a filler to densify the mortar’s microstructure, thus contributing to strength development [48]. A higher compressive strength was measured for the mold-cast MHA composites, see Fig. 6b. Two mechanisms may be attributed to this improvement; first, many MHA particles are reactive, dissolve in the alkali environment, and contribute in the formation of binding products. The extra binder increases interparticle bonding strength and compacts the end product [30,49]. Second, the remaining unreactive particles fill up the voids. The latter was quantified using X-ray μ -CT where the addition of 1.25 wt% MHA reduced both pore size and porosity of the matrix, see Fig. 7a–c. However, as shown in Fig. 5e and ef, HA/MHA increases the rheological properties of fresh mortars, e.g., storage modulus and yield stress, making them difficult to cast. This results in extra manufacturing-related porosity, e.g., during vibration and compaction. Fig. 7e visualizes the growth in pore size of 5 wt% MHA geopolymer in contrast with the unreinforced matrix, although the pores

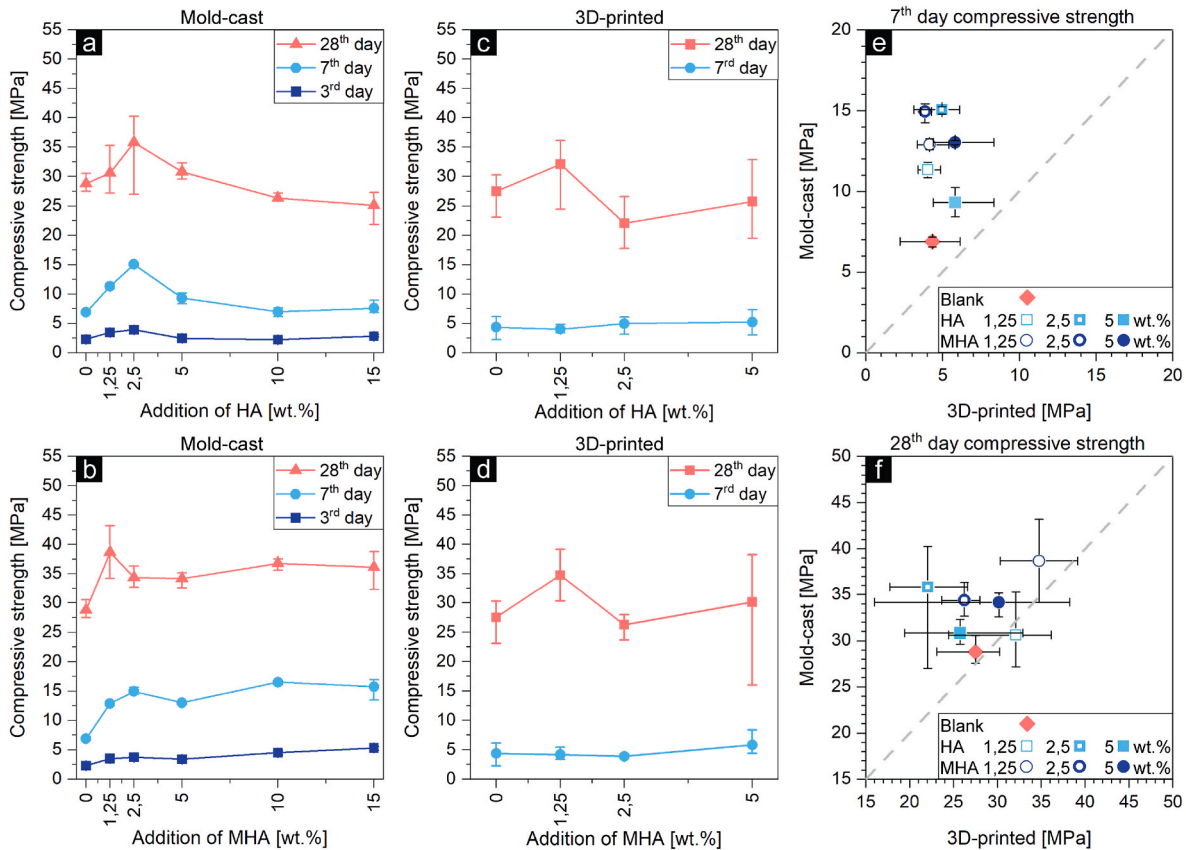


Fig. 6. Development of compressive strength as a function of time, HA/MHA concentration, and manufacturing technique; a) mold-cast HA-reinforced composites; b) mold-cast MHA-reinforced composites; c) 3D-printed HA-reinforced composites; d) 3D-printed MHA-reinforced composites; e & f) correlation between the compressive strength of mold-cast and 3D printed specimens at 7th and 28th days, respectively.

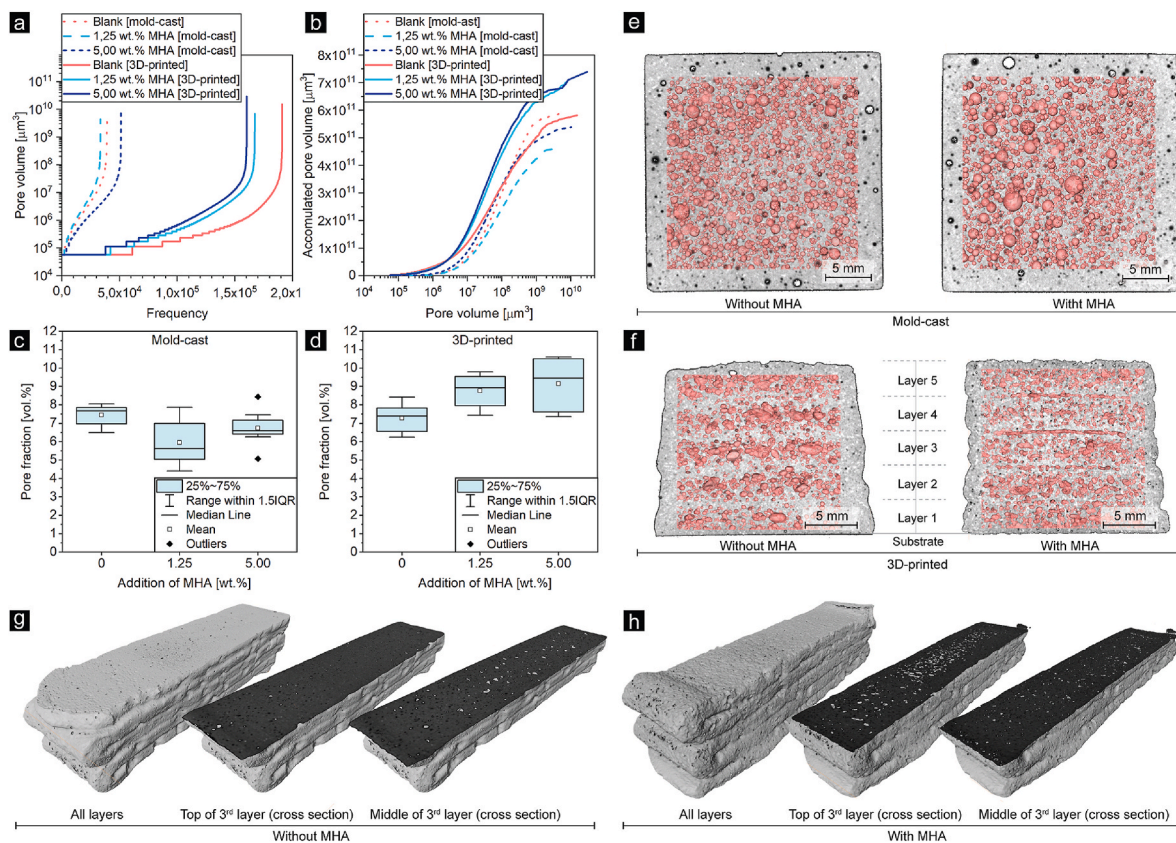


Fig. 7. X-ray μ -CT results for geopolymers composites containing a different mass of MHA; a) pore volume as a function of frequency (38.6 μm resolution); b) pore volume distribution; c & d) total porosity in mold-cast and 3D-printed specimens; e & f) visualization of pore distributions across the depth of mold-cast and 3D-printed specimens; g & h) interlayer defects (89.7 μm resolution).

were almost evenly distributed in both mold-cast samples. The induced porosity partially offsets the improving mechanisms of mechanical properties, especially at matrices with high reinforcement [50–52].

Fig. 6c and d shows the compressive strength of the 3D-printed HA-based and MHA-based geopolymer matrices, respectively. Due to rheological constraints, only mixes containing less than 5 wt% HA/MHA were tested. In general, the compressive strength of 3D printed specimens was lower than their mold-cast counterparts, mainly due to their higher porosity, compare Fig. 7c and d. Besides, the compressive strengths of the 3D-printed HA and MHA mortars were quite comparable while showing higher deviations than their corresponding mold-cast specimens. This high deviation resulted from unevenly distributed large voids with irregular shapes at the interlayer zones of the 3D-printed specimens that are increased at higher HA/MHA content matrices, see Fig. 7f–h [52–54]. These voids can negatively influence the long-term durability of the material. Notably, they can partially be eliminated by modifying the rheological properties of fresh matrices, e. g., by increasing the liquid content [22]. However, increasing the liquid content impacts materials' shrinkage and mechanical properties.

Another interesting observation was that the gap between the compressive strength of 3D-printed specimens and mold-cast ones became closer over time, compare Fig. 6e and f. A smaller compressive strength was expected for the 3D printed specimens at 7-day due to the surface dehydration that decelerates the strength development compared with those of mold-cast specimens which were covered for

three days [55–57]. However, curing the samples for a long time in similar environmental conditions (21 ± 1 °C and $\sim 50\%$ RH) regulated the rate of reactions.

The average results of flexural strength tests of HA/MHA reinforced geopolymer composites, along with the reference material, are given in Fig. 8a–f for mold-cast and 3D printed specimens. In general, the development of flexural strengths was found to follow similar trends to those of compressive strengths. Despite this, the positive effects of HA/MHA were slightly higher at the flexural properties, which micro-structurally is attributed to the tubular geometry and surface characteristic of HA/MHA particles, making them behave as micro-fibers with a strong interfacial bond with the geopolymer matrix. The SEM images in Fig. 9a–d evident the composite action of the undissolved HA and MHA with geopolymer binders [58]. However, less frequent individual MHA particles were observed in the geopolymer composites compared with their HA counterparts. A similar result was confirmed in TEM of the solid residues of dissolution reactivity tests, and tubular structures were rarely found in the MHA residues. Inevitably, the thickness of the preserved nanotubes in the residues was thinner in contrast to their initial condition, compare TEM images in Fig. 10 and 3. Therefore, partial dissolution of the nanotubes and reducing their composite action are expected over a long time. A similar mechanism is already known for glass and basalt fibers [50,59]. Besides, the aggregated MHA particles discussed in Section 3.1.2 were traceable in the geopolymer composites, see Fig. 9d. These particles almost remained unfilled, and their presence

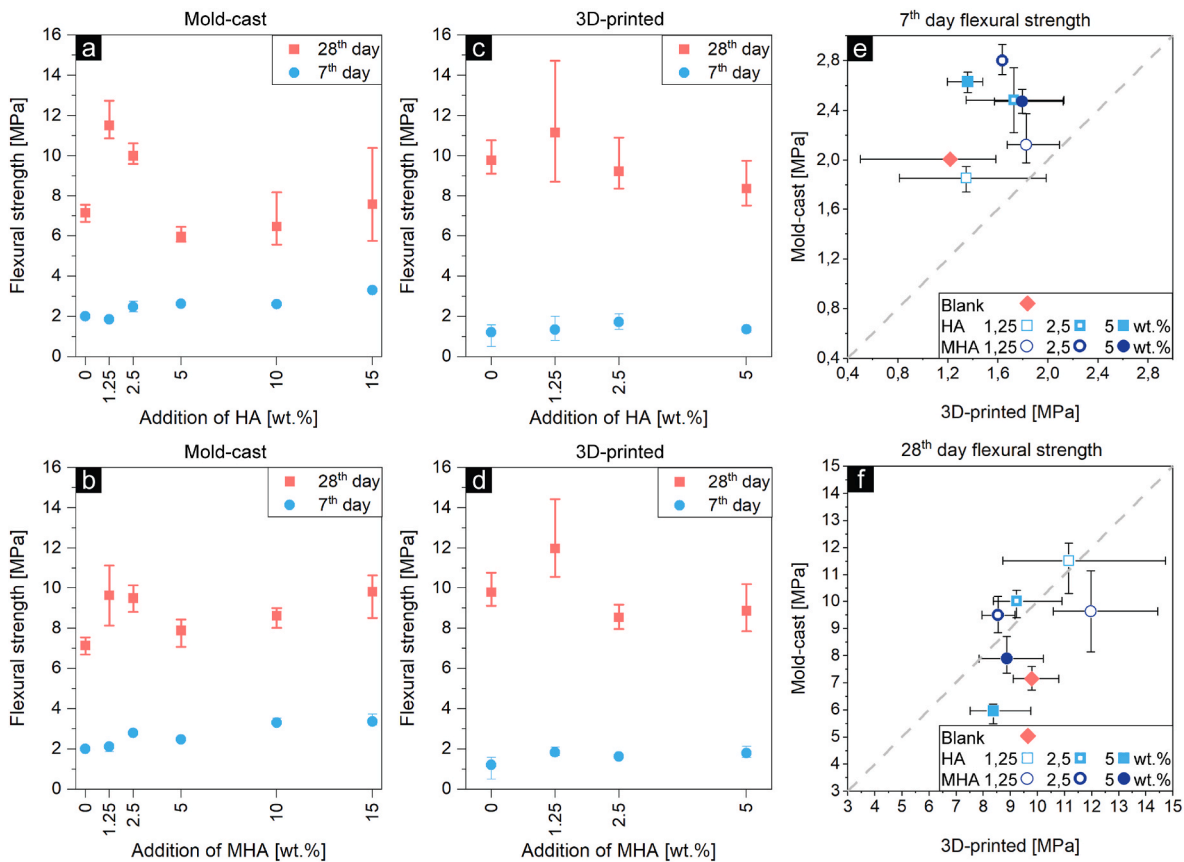


Fig. 8. Development of flexural strength as a function of time, HA/MHA concentration, and manufacturing technique; a) mold-cast HA-reinforced composites; b) mold-cast MHA-reinforced composites; c) 3D-printed HA-reinforced composites; d) 3D-printed MHA-reinforced composites; e & f) correlation between the compressive strength of mold-cast and 3D printed specimens at 7th and 28th days, respectively.

increased the risk of local fractures impacting the bulk composite’s mechanical properties [44,49–51].

Another interesting observation was that the 28-day flexural strength of the 3D printed specimens was often higher than their mold-cast counterparts (Note, the strengths in other directions might be different). This was due to anisotropy in the layered structure of 3D-printed specimens caused by the combined effects of matrix compaction and HA alignment in the extrusion direction [60–63]. However, as explained earlier, these positive effects were offset partially because of the uncontrolled surface dehydration at early ages.

4. Conclusion

This study showed the potential of using HA nanotubes as an inorganic rheological modifier agent to tune the properties of 3D printable geopolymers. It was shown that HA’s crystalline structure and phase composition are highly influenced by the thermal treatment that alters its dissolution reactivity in the alkaline environment of geopolymer. The reactivity considerably increased when HA was dehydroxylated at 800 °C, and at this stage, it accelerated the setting and shortened the printing window of the fresh geopolymer mortar. However, regardless of the reactivity, adding HA/MHA enhanced the rheological properties and buildability of the printable mortars. In addition, thermal treatment over 800 °C induced physical changes such as particle

aggregation and sintering, which are the deriving forces for increasing particle size and reducing specific surface area. In this study, the particle aggregation at 800 °C led to inhomogeneous extrusion of the fresh mortar.

A small amount of HA/MHA was shown to improve the mechanical properties of the mortars through different mechanisms. The less reactive HA remained in the hardened matrix as micro-filler and micro-fibers, while the highly reactive MHA dissolved during the reaction and produced a higher binder. However, these improving mechanisms were partially offset by the extra porosity induced in the matrix due to less workability, especially in matrices with a high concentration of HA/MHA. The aggregated particles of MHA intensified this effect. Compared with mold-cast specimens, the mechanical properties of 3D-printed specimens were lower at early ages due to their different high surface dehydration conditions. However, the gap became closer over time when the curing conditions were the same.

Declaration of competing interest

The authors declare that they have no known competing financial interests or personal relationships that could have appeared to influence the work reported in this paper.

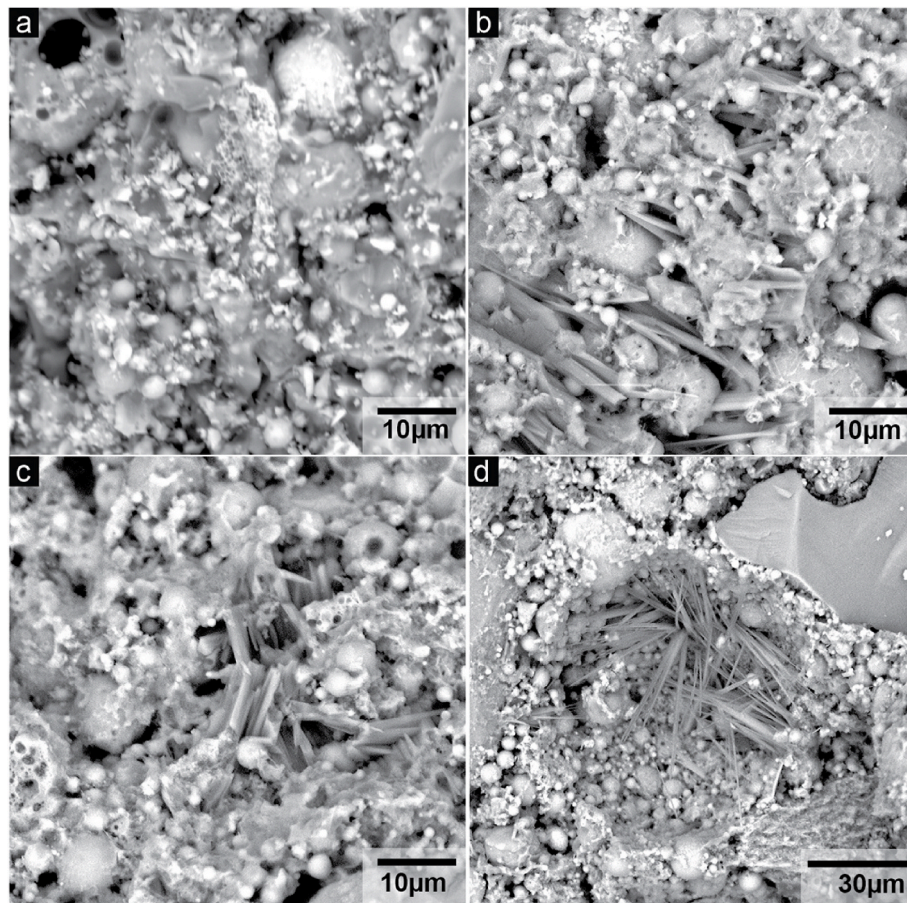


Fig. 9. SEM images of a) geopolymer mortar; b) HA-reinforced geopolymer; c & d) MHA-reinforced geopolymer.

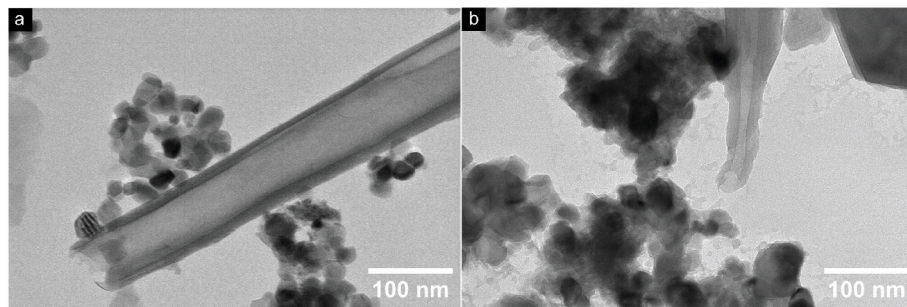


Fig. 10. TEM images of the residues of a) HA and b) MHA after dissolution in 8 M sodium hydroxide solution.

Data availability

Data will be made available on request.

Acknowledgment

N. Ranjbar would like to acknowledge the research grant (42098) from VILLUM FONDEN. M. Mehrali acknowledges financial support from VILLUM FONDEN (grant number: 00025460). We would also like to acknowledge the Danish Council for Independent Research through the DFF-Research Project1 (Thematic Research, green transition) grant with number: 0217-00263B. Transmission electron microscopy was performed at the National Centre for Nano Fabrication and Characterization at the Technical University of Denmark. The 3D Imaging Centre at the Technical University of Denmark and the Danish National Facility for Imaging with X-rays, DANFIX, funded by the Danish Agency for

Science and Higher Education, grant ID 5072-00030B. The 3D Imaging Centre at The Technical University of Denmark is gratefully acknowledged for support and access to micro-CT.

References

- [1] L. Reiter, T. Wangler, N. Roussel, R.J. Flatt, The role of early age structural build-up in digital fabrication with concrete, *Cement Concr. Res.* 112 (2018) 86–95.
- [2] F. Bos, R. Wolfs, Z. Ahmed, T. Salet, Additive manufacturing of concrete in construction: potentials and challenges of 3D concrete printing, *Virtual Phys. Prototyp.* 11 (3) (2016) 209–225.
- [3] G. Ma, R. Buswell, W.R.L. da Silva, L. Wang, J. Xu, S.Z. Jones, Technology readiness: a global snapshot of 3D concrete printing and the frontiers for development, *Cement Concr. Res.* 156 (2022), 106774.
- [4] N. Roussel, Rheological requirements for printable concretes, *Cement Concr. Res.* 112 (2018) 76–85.
- [5] K. Kondepudi, K.V. Subramaniam, B. Nematollahi, S.H. Bong, J. Sanjayan, Study of particle packing and paste rheology in alkali activated mixtures to meet the

- rheology demands of 3D Concrete Printing, *Cement Concr. Compos.* (2022), 104581.
- [6] A. Perrot, A. Pierre, V. Nerella, R. Wolfs, E. Keita, S. Nair, N. Neithalath, N. Roussel, V. Mechtcherine, From analytical methods to numerical simulations: a process engineering toolbox for 3D concrete printing, *Cement Concr. Compos.* 122 (2021), 104164.
- [7] S. Ghourchian, M. Butler, M. Krüger, V. Mechtcherine, Modelling the development of capillary pressure in freshly 3D-printed concrete elements, *Cement Concr. Res.* 145 (2021), 106457.
- [8] S. Bhattacharjee, M. Santhanam, Investigation on the effect of alkali-free aluminium sulfate based accelerator on the fresh properties of 3D printable concrete, *Cement Concr. Compos.* 130 (2022), 104521.
- [9] L. Shao, P. Feng, W. Zuo, H. Wang, Z. Geng, Q. Liu, C. Miao, Z. Liu, A novel method for improving the printability of cement-based materials: controlling the releasing of capsules containing chemical admixtures, *Cement Concr. Compos.* 128 (2022), 104456.
- [10] D. Marchon, S. Kawashima, H. Bessaies-Bey, S. Mantellato, S. Ng, Hydration and rheology control of concrete for digital fabrication: potential admixtures and cement chemistry, *Cement Concr. Res.* 112 (2018) 96–110.
- [11] J. Davidovits, Geopolymers: inorganic polymeric new materials, *J. Therm. Anal. Calorim.* 37 (8) (1991) 1633–1656.
- [12] N. Ranjbar, C. Kuenzel, J. Spangenberg, M. Mehrali, Hardening evolution of geopolymers from setting to equilibrium: a review, *Cement Concr. Compos.* 114 (2020), 103729.
- [13] P. Duxson, A. Fernández-Jiménez, J.L. Provis, G.C. Lukey, A. Palomo, J.S. van Deventer, Geopolymer technology: the current state of the art, *J. Mater. Sci.* 42 (9) (2007) 2917–2933.
- [14] B. Walkley, X. Ke, O.H. Hussein, S.A. Bernal, J.L. Provis, Incorporation of strontium and calcium in geopolymer gels, *J. Hazard Mater.* 382 (2020), 121015.
- [15] P. Duxson, S.W. Mallicoat, G.C. Lukey, W.M. Kriven, J.S.J. van Deventer, The effect of alkali and Si/Al ratio on the development of mechanical properties of metakaolin-based geopolymers, *Colloids Surf. Physicochem. Eng. Aspects* 292 (1) (2007) 8–20.
- [16] A. Fernández-Jiménez, A. Palomo, I. Sobrados, J. Sanz, The role played by the reactive alumina content in the alkaline activation of fly ashes, *Microporous Mesoporous Mater.* 91 (1–3) (2006) 111–119.
- [17] A. Fernández-Jiménez, A. Palomo, M. Criado, Microstructure development of alkali-activated fly ash cement: a descriptive model, *Cement Concr. Res.* 35 (6) (2005) 1204–1209.
- [18] Á. Palomo, S. Alonso, A. Fernandez-Jiménez, I. Sobrados, J. Sanz, Alkaline activation of fly ashes: NMR study of the reaction products, *J. Am. Ceram. Soc.* 87 (6) (2004) 1141–1145.
- [19] A. Favier, G. Habert, J.B. d'Espinoise de Lacaillerie, N. Roussel, Mechanical properties and compositional heterogeneities of fresh geopolymer pastes, *Cement Concr. Res.* 48 (2013) 9–16.
- [20] A. Favier, G. Habert, N. Roussel, J.-B. d'Espinoise de Lacaillerie, A multinuclear static NMR study of geopolymerisation, *Cement Concr. Res.* 75 (2015) 104–109.
- [21] A. Fernández-Jiménez, A. Palomo, I. Sobrados, J. Sanz, The role played by the reactive alumina content in the alkaline activation of fly ashes, *Microporous Mesoporous Mater.* 91 (1) (2006) 111–119.
- [22] N. Ranjbar, M. Mehrali, C. Kuenzel, C. Gundlach, D.B. Pedersen, A. Dolatshahi-Pirouz, J. Spangenberg, Rheological characterization of 3D printable geopolymers, *Cement Concr. Res.* 147 (2021), 106498.
- [23] S.H. Bong, M. Xia, B. Nematollahi, C. Shi, Ambient temperature cured 'just-add-water' geopolymer for 3D concrete printing applications, *Cement Concr. Compos.* 121 (2021), 104060.
- [24] B. Panda, C. Unluer, M.J. Tan, Extrusion and rheology characterization of geopolymer nanocomposites used in 3D printing, *Compos. B Eng.* 176 (2019), 107290.
- [25] B. Nematollahi, P. Vijay, J. Sanjayan, A. Nazari, M. Xia, V. Naidu Nerella, V. Mechtcherine, Effect of polypropylene fibre addition on properties of geopolymers made by 3D printing for digital construction, *Materials* 11 (12) (2018) 2352.
- [26] J.I. Dawson, R.O. Oreffo, Clay: new opportunities for tissue regeneration and biomaterial design, *Adv. Mater.* 25 (30) (2013) 4069–4086.
- [27] S. Murugesan, T. Scheibel, Copolymer/clay nanocomposites for biomedical applications, *Adv. Funct. Mater.* 30 (17) (2020), 1908101.
- [28] E. García-Romero, M. Suárez, Sepiolite-palygorskite polysomatic series: oriented aggregation as a crystal growth mechanism in natural environments, *Am. Mineral.* 99 (8–9) (2014) 1653–1661.
- [29] P. Yuan, D. Tan, F. Annabi-Bergaya, Properties and applications of halloysite nanotubes: recent research advances and future prospects, *Appl. Clay Sci.* 112 (2015) 75–93.
- [30] C.R. Kaze, T. Alomayri, A. Hasan, S. Tome, G.L. Lecomte-Nana, J.G.D. Nemaleu, H. K. Tchakoute, E. Kamseu, U.C. Melo, H. Rahier, Reaction kinetics and rheological behaviour of meta-halloysite based geopolymer cured at room temperature: effect of thermal activation on physicochemical and microstructural properties, *Appl. Clay Sci.* 196 (2020), 105773.
- [31] H. Asgar, J. Jin, J. Miller, I. Kuzmenko, G. Gadikota, Contrasting thermally-induced structural and microstructural evolution of aluminosilicates with tubular and planar arrangements: case study of halloysite and kaolinite, *Colloids Surf. A Physicochem. Eng. Asp.* 613 (2021), 126106.
- [32] P. Yuan, D. Tan, F. Aannabi-Bergaya, W. Yan, M. Fan, D. Liu, H. He, Changes in structure, morphology, porosity, and surface activity of mesoporous halloysite nanotubes under heating, *Clay Clay Miner.* 60 (6) (2012) 561–573.
- [33] C. Kuenzel, N. Ranjbar, Dissolution mechanism of fly ash to quantify the reactive aluminosilicates in geopolymerisation, *Resour. Conserv. Recycl.* 150 (2019), 104421.
- [34] N. Ranjbar, C. Kuenzel, Influence of preheating of fly ash precursors to produce geopolymers, *J. Am. Ceram. Soc.* 100 (7) (2017) 3165–3174.
- [35] J. Ouyang, Z. Zhou, Y. Zhang, H. Yang, High morphological stability and structural transition of halloysite (Hunan, China) in heat treatment, *Appl. Clay Sci.* 101 (2014) 16–22.
- [36] C.R. Kaze, H.K. Tchakoute, T.T. Mbakop, J.R. Mache, E. Kamseu, U.C. Melo, C. Leonelli, H. Rahier, Synthesis and properties of inorganic polymers (geopolymers) derived from Cameroon-meta-halloysite, *Ceram. Int.* 44 (15) (2018) 18499–18508.
- [37] B. Zhang, H. Guo, P. Yuan, Y. Li, Q. Wang, L. Deng, D. Liu, Geopolymerization of halloysite via alkali-activation: dependence of microstructures on precalcination, *Appl. Clay Sci.* 185 (2020), 105375.
- [38] J.N.Y. Djobo, A. Elimbi, H.K. Tchakouté, S. Kumar, Mechanical activation of volcanic ash for geopolymer synthesis: effect on reaction kinetics, gel characteristics, physical and mechanical properties, *RSC Adv.* 6 (45) (2016) 39106–39117.
- [39] S. Kumar, R. Kumar, Mechanical activation of fly ash: effect on reaction, structure and properties of resulting geopolymer, *Ceram. Int.* 37 (2) (2011) 533–541.
- [40] J. Sanz, A. Madani, J. Serratos, J. Moya, S. Aza, Aluminum-27 and Silicon-29 magic-angle spinning nuclear magnetic resonance study of the kaolinite-mullite transformation, *J. Am. Ceram. Soc.* 71 (10) (1988) C418–C421.
- [41] J. Rocha, J. Klinowski, Solid-state NMR studies of the structure and reactivity of metakaolinite, *Angew. Chem. Int. Ed. Engl.* 29 (5) (1990) 553–554.
- [42] K.J. MacKenzie, D.R. Brew, R.A. Fletcher, R. Vagana, Formation of aluminosilicate geopolymers from 1: 1 layer-lattice minerals pre-treated by various methods: a comparative study, *J. Mater. Sci.* 42 (12) (2007) 4667–4674.
- [43] A. Kazemian, X. Yuan, E. Cochran, B. Khoshnevis, Cementitious materials for construction-scale 3D printing: laboratory testing of fresh printing mixture, *Construct. Build. Mater.* 145 (2017) 639–647.
- [44] S. Kawashima, K. Wang, R.D. Ferron, J.H. Kim, N. Tregger, S. Shah, A review of the effect of nanoclays on the fresh and hardened properties of cement-based materials, *Cement Concr. Res.* 147 (2021), 106502.
- [45] M. Chougan, S.H. Ghaffar, B. Nematollahi, P. Sikora, T. Dorn, D. Stephan, A. Albar, M.J. Al-Kheetan, Effect of natural and calcined halloysite clay minerals as low-cost additives on the performance of 3D-printed alkali-activated materials, *Mater. Des.* 223 (2022), 111183.
- [46] C.A. Rees, J.L. Provis, G.C. Lukey, J.S. Van Deventer, The mechanism of geopolymer gel formation investigated through seeded nucleation, *Colloids Surf. A Physicochem. Eng. Asp.* 318 (1–3) (2008) 97–105.
- [47] Q. Wan, F. Rao, S. Song, Reexamining calcination of kaolinite for the synthesis of metakaolin geopolymers-roles of dehydroxylation and recrystallization, *J. Non-Cryst. Solids* 460 (2017) 74–80.
- [48] N. Farzadnia, A.A.A. Ali, R. Demirboga, M.P. Anwar, Effect of halloysite nanoclay on mechanical properties, thermal behavior and microstructure of cement mortars, *Cement Concr. Res.* 48 (2013) 97–104.
- [49] Z. Zhang, H. Wang, X. Yao, Y. Zhu, Effects of halloysite in kaolin on the formation and properties of geopolymers, *Cement Concr. Compos.* 34 (5) (2012) 709–715.
- [50] N. Ranjbar, M. Zhang, Fiber-reinforced geopolymer composites: a review, *Cement Concr. Compos.* 107 (2020), 103498.
- [51] N. Ranjbar, M. Mehrali, A. Behnia, A. Javadi Pordsari, M. Mehrali, U.J. Alengaram, M.Z. Jumaat, A comprehensive study of the polypropylene fiber reinforced fly ash based geopolymer, *PLoS One* 11 (1) (2016), e0147546.
- [52] M. van den Heever, A. du Plessis, J. Kruger, G. van Zijl, Evaluating the effects of porosity on the mechanical properties of extrusion-based 3D printed concrete, *Cement Concr. Res.* 153 (2022), 106695.
- [53] Z. Geng, W. She, W. Zuo, K. Lyu, H. Pan, Y. Zhang, C. Miao, Layer-interface properties in 3D printed concrete: dual hierarchical structure and micromechanical characterization, *Cement Concr. Res.* 138 (2020), 106220.
- [54] J. Kruger, A. du Plessis, G. van Zijl, An investigation into the porosity of extrusion-based 3D printed concrete, *Addit. Manuf.* 37 (2021), 101740.
- [55] R. Wolfs, F. Bos, T. Salet, Hardened properties of 3D printed concrete: the influence of process parameters on interlayer adhesion, *Cement Concr. Res.* 119 (2019) 132–140.
- [56] E. Keita, H. Bessaies-Bey, W. Zuo, P. Belin, N. Roussel, Weak bond strength between successive layers in extrusion-based additive manufacturing: measurement and physical origin, *Cement Concr. Res.* 123 (2019), 105787.
- [57] Y. Weng, M. Li, D. Zhang, M.J. Tan, S. Qian, Investigation of interlayer adhesion of 3D printable cementitious material from the aspect of printing process, *Cement Concr. Res.* 143 (2021), 106386.
- [58] T. Vincent, A. Gholampour, T. Ozbakkaloglu, T.D. Ngo, Waste-based alkali-activated mortars containing low-and high-halloysite kaolin nanoparticles, *J. Clean. Prod.* 327 (2021), 129428.
- [59] B. Wei, H. Cao, S. Song, Tensile behavior contrast of basalt and glass fibers after chemical treatment, *Mater. Des.* 31 (9) (2010) 4244–4250.

- [60] T.T. Le, S.A. Austin, S. Lim, R.A. Buswell, R. Law, A.G. Gibb, T. Thorpe, Hardened properties of high-performance printing concrete, *Cement Concr. Res.* 42 (3) (2012) 558–566.
- [61] A.R. Arunothayan, B. Nematollahi, R. Ranade, J.G. Sanjayan, K.H. Khayat, Fiber orientation effects on ultra-high performance concrete formed by 3D printing, *Cement Concr. Res.* 143 (2021), 106384.
- [62] V.C. Li, F.P. Bos, K. Yu, W. McGee, T.Y. Ng, S.C. Figueiredo, K. Nefs, V. Mechtcherine, V.N. Nerella, J. Pan, On the emergence of 3D printable engineered, strain hardening cementitious composites (ECC/SHCC), *Cement Concr. Res.* 132 (2020), 106038.
- [63] K. Wi, K. Wang, P.C. Taylor, S. Laflamme, S. Sritharan, H. Qin, Properties and microstructure of extrusion-based 3D printing mortar containing a highly flowable, rapid set grout, *Cement Concr. Compos.* 124 (2021), 104243.